PHOTONICS Research

Silicon-integrated nonlinear III-V photonics

WEIQIANG XIE,[1,2,†] CHAO XIANG,[1,†] LIN CHANG,[1] WARREN JIN,[1] JONATHAN PETERS,[1] AND JOHN E. BOWERS[1,*]

[1]*Department of Electrical and Computer Engineering, University of California, Santa Barbara, Santa Barbara, California 93106, USA*
[2]*Current address: Department of Electronic Engineering, Shanghai Jiao Tong University, Shanghai 200240, China*
*Corresponding author: bowers@ece.ucsb.edu

Mainstream silicon photonic integrated circuits are based on compact and low-loss silicon-on-insulator (SOI) waveguide platforms. However, monolithic SOI-based photonics provides only a limited number of functional device types. Here, to extend the on-chip capabilities, we propose a general heterogeneous integration approach to embed highly nonlinear III-V (AlGaAs) photonics into the SOI platform. We develop low-loss AlGaAs-on-SOI photonic circuits with integrated Si waveguides and showcase sub-milliwatt-threshold (∼0.25 mW) Kerr frequency comb generation in ultrahigh-Q AlGaAs microrings (Q over 10^6) at the telecom bands. Our demonstration complements existing mature Si photonics technology with efficient nonlinear functionalities provided by III-V and propels conventional Si photonics into emerging nonlinear photonic applications towards fully chip-based nonlinear engines. © 2022 Chinese Laser Press

https://doi.org/10.1364/PRJ.446898

1. INTRODUCTION

Silicon photonics based on silicon-on-insulator (SOI) substrates has been rapidly growing over the past two decades, providing various on-chip passive/active photonic functionalities (waveguide-based passive components, modulators, photodetectors, etc.) by taking advantage of mature planar CMOS technology, leading to the development of Si photonic integrated circuits (PICs) [1–4]. Moreover, III–V-on-Si (III-V/Si) heterogeneous integration techniques have been developed to address the laser source issue for Si photonics and have now been adopted in scalable state-of-the-art CMOS-compatible processes [5]. Today, Si photonics is playing a leading role in the community of integrated photonics and has found applications in a large number of areas including optical interconnects [6,7], telecommunications [8], computing [9], and so on [10]. Meanwhile, significant progress spanning the last decade on integrated nonlinear photonics has emerged as a new paradigm for both nonlinear optics research and applications. An intriguing offering of integrated nonlinear photonics is its capability of generating new classes of coherent, ultra-broadband light sources (i.e., microcombs) in nonlinear waveguides [11,12], which is not attainable from linear photonics systems. Microcombs have triggered widespread use of chip-scale nonlinear devices in applications [13] including ultrahigh-capacity coherent telecommunications [14,15], optical frequency synthesis [16], optical atomic clocks [17], quantum optics [18], etc. In the past few years, significant technological advances have enabled ultralow-loss nonlinear waveguides and ultrahigh-quality-factor (Q-factor) microresonators [19–23].

Those breakthroughs have essentially allowed high-efficiency nonlinear processes operating at dramatically reduced power levels of milliwatts or sub-milliwatts [19,21,24–28], eliminating bulky optical equipment such as benchtop pump lasers and amplifiers. The power requirements in nonlinear waveguides are now compatible with co-integrated III-V/Si pump lasers on a single chip [29], which represents a key step towards harnessing the on-chip nonlinear properties from individual and passive-only nonlinear devices, to mass-manufactured system-level architectures and application developments.

Therefore, it is naturally desired to embed nonlinear functionalities in relatively mature Si PICs for complete chip-scale nonlinear photonics with the ability of direct signal generation and processing. However, Si has inherent disadvantages regarding many nonlinear applications, such as its small-bandgap-induced strong two-photon absorption (TPA) and related free-carrier losses at telecom wavelengths and insignificant $\chi^{(2)}$ nonlinearity [30–32], thus limiting its nonlinear efficiency and available functionality at telecom wavelength bands where other photonic applications are clustered. Consequently, there is a strong need to look for an alternative nonlinear material candidate that is perfectly suited for compatibility with Si photonics integration and adding the missing piece. Among various investigated integrated nonlinear platforms from dielectrics to semiconductors [33–43], aluminum gallium arsenide (AlGaAs) is particularly attractive, due to its strong intrinsic second- and third-order nonlinearities, relatively large and tailorable bandgap, and large linear refractive index similar to Si that can

ensure strong photon confinement and also efficient coupling to Si PICs. In particular, the bandgap can be engineered from about 1.42 eV to 2.95 eV by varying the alloy composition of $Al_xGa_{1-x}As$ [44] so that the operating wavelengths can be sufficiently below the half-bandgap wavelength, thus allowing mitigation of the most detrimental nonlinear losses induced by TPA effects [45,46]. For example, by choosing the Al composition to be around 0.2, the corresponding bandgap is 1.69 eV, which results in a TPA cutoff wavelength of 1467 nm, and thus the TPA can be ignored when operating at the telecom band around 1550 nm [42,47–49]. This advantage overcomes the intrinsic detrimental TPA effect in Si that hinders its nonlinear applications. As a consequence, AlGaAs promises ideal nonlinear optical figures of merit alongside linear Si photonics [50,51], and has long been termed as the "the silicon of nonlinear optical materials" at telecom bands [45]. Moreover, recently, the rapid growth of implementing these superior nonlinearities has been taking place by using an AlGaAs-on-insulator (AlGaAsOI) platform [42,43,52], which enables compact, high-confinement, ultralow-loss waveguides and microresonators. Thus, various on-chip ultra-efficient nonlinear applications have been unlocked including second-harmonic generation [53,54], super-continuum generation [55], Kerr frequency comb/soliton generation (threshold powers of the order of 20 μW) [21,56,57], and ultra-bright entangled-photon-pair generation [58].

Here, we further extend the integration of AlGaAs nonlinear photonics onto an SOI substrate with the goal of bridging "the silicon of nonlinear optical materials" and Si PICs. To achieve this goal, we propose a general heterogeneous architecture to combine the two types of PICs with fabrication compatibility and integration scalability. We demonstrate

low-loss AlGaAs-on-SOI waveguides and microresonators with Q-factors over 10^6, as well as low coupling loss (<1 dB) between AlGaAs and Si PICs. Efficient microcomb generation on a standard SOI platform using a telecom-band pump is reported for the first time, with a threshold power of as low as ~0.25 mW. Particularly, the pump and access of the microcomb are through Si waveguides. The demonstrated compatibility in both the fabrication process and power budget for the two classes of photonic functionalities unfolds the possibility of fully integrated scalable and advanced nonlinear PICs, by leveraging both the mature technology of Si photonics and superior nonlinear properties of AlGaAs.

2. DESIGN AND FABRICATION

Figure 1(a) depicts the proposed device configuration whereby light in the bottom SOI layer is coupled to the top AlGaAs layer and vice versa via evanescent coupling aided by a pair of inverse tapers of Si and AlGaAs waveguides. The two device layers are spaced by an oxide layer of certain thickness (200 nm in current case). In practice, this structure can be realized by low-temperature (typically < 400°C) wafer bonding of AlGaAs on a waveguide-patterned SOI wafer. More generally, such vertical, heterogeneous integration of AlGaAs PICs can be performed on a Si photonics substrate in which critical processes are completed for both passive and active components including waveguides, Si PN junction-based modulators, SiGe detectors, etc. Therefore, the proposed integration strategy possesses the capability of integrating high-quality nonlinear AlGaAs PICs on a fully functional Si PIC wafer in a back-end-of-line (BEOL) integration approach for large-scale and advanced PICs. It has to be noted that the BEOL integration of AlGaAs is fully
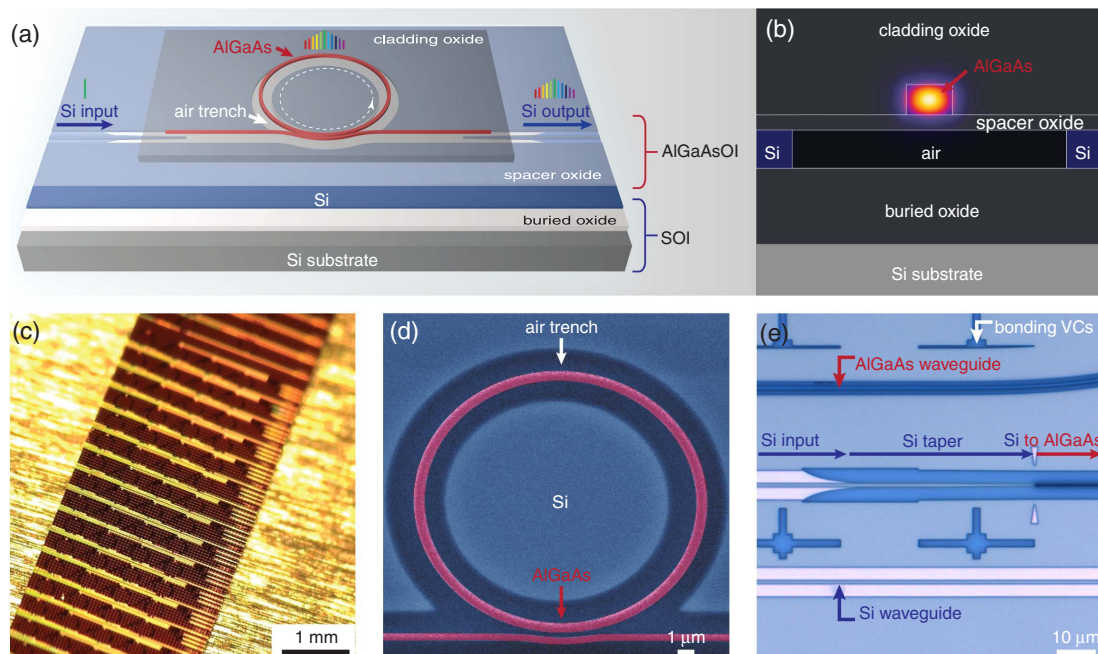

Fig. 1. AlGaAs-Si heterogeneous nonlinear photonics integration. (a) Schematic of the AlGaAs-Si integration architecture. (b) Simulated TE0 mode profile of AlGaAs waveguide on SOI with spacer oxide and air trench. (c) Photograph of the fabricated chip containing 100G FSR devices diced from a 100 mm diameter SOI wafer. (d) False-colored SEM image of a fabricated suspended AlGaAs microring. (e) Optical microscope image of the Si-AlGaAs taper.

compatible with the existing Si PIC process flow without modifying the thermal budget, distinguishing itself from silicon nitride-based nonlinear photonics, which normally requires high-temperature anneals. Here, for the purpose of proof-of-concept demonstration, the simple Si waveguide elements are defined for off-chip coupling access, while in the AlGaAs layer, a bus-waveguide coupled microring resonator is defined. The Si underneath the AlGaAs waveguides and resonators is removed to avoid mode leakage, resulting in a suspended structure above an air trench as shown in Fig. 1(b). Note that this air trench can also be filled with oxide, followed by chemical mechanical polishing for surface planarization. The input/output Si waveguide is shallow etched by ~231 nm on an SOI substrate with a 500 nm Si layer and 1.0 μm buried oxide layer. In the coupling region, a shallow-etched Si waveguide is transitioned to a deep-etched Si waveguide with full 500 nm etch depth. In addition, cross-shaped vertical channels (VCs) are patterned on the Si layer to facilitate AlGaAs bonding with an improved yield. A 400 nm thick AlGaAs film is grown by molecular-beam epitaxy, and the aluminum composition is chosen to be 20% so that the TPA effect is negligible at wavelengths around 1550 nm, as discussed above. After bonding, the fully etched AlGaAs microrings are defined with different radii and widths in a range of 600 nm to 750 nm to ensure anomalous group-velocity dispersion (GVD) around 1550 nm, as previously demonstrated for Kerr frequency comb generation [43]. The bus waveguide is carefully designed to allow efficient coupling to the desired fundamental transverse-electric (TE0) mode. Note that initially the choice of Si thickness (500 nm) is considered to accommodate the co-integration of heterogeneous InP/Si lasers [29]. Nevertheless, the proposed integration architecture is also applicable to other SOI substrates with different Si thicknesses (e.g., 220 nm), as well as different AlGaAs thicknesses. The field profile of the TE0 mode in the AlGaAs waveguide is shown in Fig. 1(b), indicating a tight mode confinement within the AlGaAs core. To optimize the coupling between Si and AlGaAs tapers, we performed numerical simulation for the transmission of the TE0 mode and chose the widths of Si and AlGaAs to be 200 nm and 300 nm, respectively, the length to be 200 μm, and the oxide thickness to be 200 nm with a theoretical coupling efficiency >95%. Figures 1(c)–1(e) show the images of the fabricated

AlGaAs/Si heterogeneously integrated device, indicating the chip-scale fabrication throughput, the realized AlGaAs/Si structure, and the coupling tapers between Si and AlGaAs.

In Fig. 2, we present the simplified fabrication process. The overall fabrication consists of three major steps: Si waveguide patterning on the SOI wafer, AlGaAs epi wafer bonding, and AlGaAs waveguide patterning [Fig. 2(a)]. The details of the process flow are shown in Fig. 2(b). For the entire process, a 248 nm deep ultraviolet (DUV) stepper was used for photolithography, which is well suited for scalable integration and volume fabrication. The fabrication started with the deposition of 200 nm oxide on a 100-mm-diameter SOI wafer using plasma-enhanced chemical vapor deposition (PECVD). The oxide layer was then patterned and dry etched with chemistries of $CHF_3/CF_4/O_2$ in inductively coupled plasma reactive-ion etching (ICP-RIE). The oxide served as a hard mask, and the Si rib waveguide was formed by dry etching ~231 nm of the 500 nm SOI in another ICP-RIE process with chemistries of SF_6/C_4F_8. Next, the fully etched Si taper was realized by a second etch of the rest of Si using a photoresist mask together with the predefined oxide mask. After Si waveguide processing, the remaining oxide mask was removed by a dip in buffered hydrogen fluoride (BHF) solution, and the wafer was carefully cleaned for the following bonding process. The second step is to bond the AlGaAs film onto the patterned Si waveguide wafer. The 400 nm thick epitaxial AlGaAs film was grown on a GaAs substrate with an etch-stop layer of 500 nm thick $Al_{0.8}Ga_{0.2}As$ in between. Here we employed a similar bonding process as reported in our previous work [21]. Different from our previous work, here we deposit 200 nm silicon dioxide on the as-grown AlGaAs surface before bonding using an optimized ICP-PECVD process, which results in a smooth deposited surface with a root-mean-squared roughness of ~0.3 nm. This oxide layer serves as a spacer for optimal coupling as well as for mechanical support of the suspended AlGaAs structures [as shown in Fig. 1(b)]. Additionally, in this work, we omit atomic layer deposition of a thin Al_2O_3 (alumina) passivation layer on the AlGaAs surface, as the combination of high stress in the oxide spacer layer and poor adhesion in the alumina passivation layer led to cracking and delamination of the deposited films. However, the absence of alumina passivation may result in slightly increased optical loss due to surface absorption.
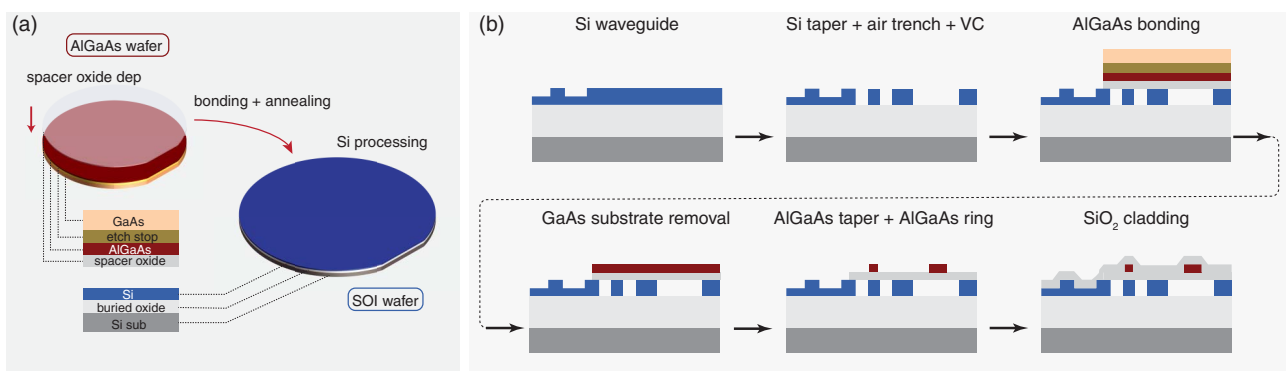

Fig. 2. Simplified schematic of the device fabrication process. (a) Device process overview and cross sectional SOI wafer and AlGaAs epi layer details. (b) Cross sectional schematics of the full process including: Si waveguide formation, Si taper/air trench/VC formation, AlGaAs bonding, GaAs substrate removal, AlGaAs taper/ring formation, and SiO_2 cladding deposition.

We note that this spacer oxide deposition could be eliminated by using chemical–mechanical planarization of the Si-photonic substrate, a technique that is widely available in standard CMOS foundries. Prior to bonding, the surfaces of the substrates were activated in O_2 plasma. The bonding was carried out at a temperature of 200°C for 10 h. We note that the same process is compatible with bonding an InP epitaxial film, which will be certainly useful for future heterogeneous integration of laser sources simultaneously with AlGaAs. The GaAs substrate was removed by a combination of mechanical lapping and wet etching in a mixture of H_2O_2 and NH_4OH at room temperature. The etch-stop layer was selectively etched in diluted HF. After bonding, the AlGaAs waveguides were then patterned using our previously optimized processes for low-loss AlGaAs waveguides [21] and finally cladded with a 1.0 μm PECVD SiO_2.

3. DEVICE CHARACTERIZATION

We first characterized the transmission spectral response of our devices. TE polarized light from a tunable laser was coupled into one Si waveguide through a lensed fiber, and the output was collected by another lensed fiber from the other Si waveguide edge coupler, as denoted in Fig. 1(a). The transmitted power was detected with a high-speed photodetector, and the response was recorded using an oscilloscope. The spectral resolution of our measurement is 0.01 pm. The input power can be further adjusted with a variable optical attenuator. Figure 3(a) shows the transmission spectra of several waveguides with the same input/output Si edge couplers connected by a series of Si-AlGaAs tapers (two, four, and six tapers) and a pure Si waveguide (zero tapers) for reference. We extracted the

taper loss at the wavelength of 1550 nm with a linear fit of the transmission as a function of the number of tapers in dB scale and show the results in Fig. 3(b), indicating a Si-AlGaAs taper loss of 0.87 dB, e.g., a coupling efficiency of 82%. For comparison, we also show the simulated taper transmission in the inset of Fig. 3(a) with a theoretical coupling efficiency of 95% at 1550 nm. Additionally, the effect of lateral misalignment between the tapers is also simulated, indicating a tolerance of at least 100 nm for <1 dB loss increment. Improvements on the taper dimension control as well as alignment accuracy can be done to further improve the coupling efficiency.

The waveguide dispersion and the Q-factors of AlGaAs microrings were obtained by measuring the transmission of the waveguide-coupled resonator devices. For the GVD characterization, using a microring with free-spectral range (FSR) of 0.5 THz and a nominal width of ∼650 nm, we measure the resonance frequencies of the TE0 mode family as a function of the relative mode number μ, relative to a reference resonance at ω_0 around 1550 nm. The resonance frequencies ω_μ of the modes can be expanded as $\omega_\mu = \omega_0 + \mu D_1 + \frac{1}{2}\mu^2 D_2 + \cdots$, where $D_1/2\pi$ is the FSR around ω_0, and $D_2/2\pi$ is related to the second-order dispersion and is positive (negative) corresponding to anomalous (normal) GVD. By fitting the data as shown in Fig. 3(c), $D_2/2\pi$ is extracted to be 62.8 MHz, indicating the anomalous dispersion for the AlGaAs waveguides. The intrinsic Q_0 are measured to be 0.97×10^6 and 1.12×10^6 for a small ring (radius of 12 μm and FSR of 1 THz) and a large ring (radius of 143 μm and FSR of 90 GHz), respectively, as shown in Figs. 3(d) and 3(e). Here the Q-factors are lower than that of our previous work [21,43], which is likely due to the bottom spacer oxide passivation and can be improved by optimizing the passivation quality. Nonetheless, the demonstrated
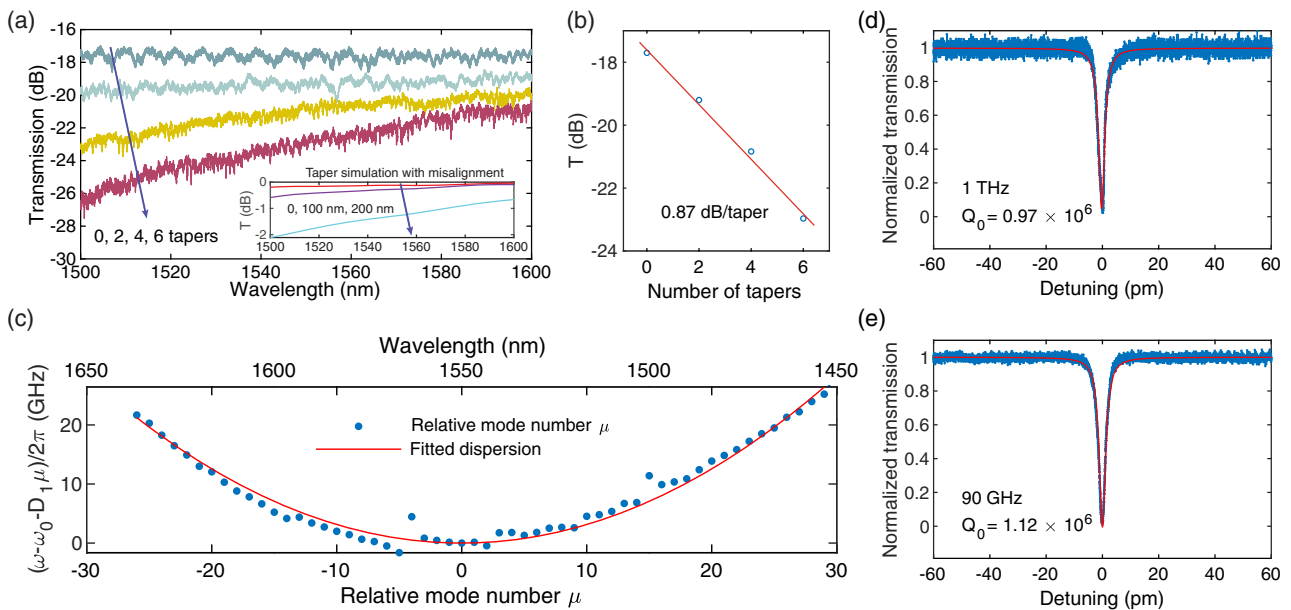

Fig. 3. Characterization of AlGaAs-Si integrated devices. (a) Measured transmission spectra of waveguides with pairs of Si-AlGaAs tapers together with the transmission of a Si waveguide for reference. Inset: simulated transmission of the Si-AlGaAs taper under different lateral misalignments. (b) Measured transmission at 1550 nm versus number of Si-AlGaAs tapers. (c) Dispersion of the TE0 mode as a function of relative mode number for a 0.5 THz FSR microring. Transmission spectra and measured intrinsic Q_0 factors of resonances at 1532.86 nm and 1521.72 nm for (d) microring with a radius of 12 μm and width of 650 nm and (e) microring with a radius of 143 μm and width of 650 nm, respectively.

Q-factor reveals a propagation loss as low as 0.5 dB/cm in the AlGaAs-on-SOI waveguides, which is also on par with the state-of-the-art result in Si PICs.

To further highlight the capability of efficient nonlinear applications in the developed AlGaAs-SOI platform, we performed a frequency comb generation experiment, in which the pump laser was injected to the AlGaAs ring through the input Si waveguide edge coupler, and the comb spectrum was collected from the output Si waveguide edge coupler. For the ring with an FSR of 1 THz, we pumped a resonance at ~1550 nm ($Q_0 \sim 0.81 \times 10^6$) and recorded the output spectra at different pump powers in the AlGaAs bus waveguide. With a pump power of about 0.25 mW, the primary sidebands of optical parametric oscillation are clearly observed at locations corresponding to multiples of the resonator FSR, as shown in Fig. 4(a). When increasing the pump power to 0.4 mW, a primary comb at a 3× FSR spacing emerges and covers a wavelength range of ~175 nm, as shown in Fig. 4(b). With a pump power of 3 mW, a complete comb at single FSR spacing is formed, spanning a broad wavelength range from 1450 nm to 1700 nm, as shown in Fig. 4(c). This is also evidence of chaotic comb generation, and better control of thermo-optic effects could lead to coherent soliton microcombs at similar power levels [56]. While several techniques could be helpful to overcome the thermal problem to achieve coherent mode-locked microcombs including using an auxiliary laser heating for temperature compensation [59] or operating the microring at very low temperatures to suppress the thermal effect [56], a more practical approach is to engineer a resonator with normal dispersion, which will reduce the impact of thermal effects on soliton formation, and has been demonstrated in our recent work [57] and can also be employed in future designs for the AlGaAs-SOI platform.

Additionally, we estimated the comb threshold power theoretically, using the expression [60] $P_{th} \approx 1.54 \left(\frac{\pi}{2}\right) \cdot \frac{Q_c}{2Q_L} \cdot \frac{n^2\, V}{n_2 \lambda Q_L^2}$, where λ is the pump wavelength, n is the modal refractive index, n_2 is the nonlinear refractive index, V is the mode volume, and Q_c and Q_L are the coupling and loaded quality factors of the resonator, respectively. Given a critical coupling condition with $Q_c = 2Q_L = Q_0$ and the measured intrinsic Q_0, the theoretical threshold power is 0.07 mW, which is lower than that observed in the measurement. This can be attributed to lower average Q factors over all resonances and the stepwise wavelength tuning approach with less resolution. Lower threshold powers are thus expected by improving the overall Q factors and using fast wavelength sweeps. Finally, we also tested the ring with 143 μm radius (FSR of 90 GHz) at the resonance of ~1550 nm ($Q_0 \sim 1.0 \times 10^6$) and show the comb spectrum at the pump power of ~15.8 mW in Fig. 4(d), in which the comb lines are almost complete over the whole span, suggesting that such power levels can sustain a coherent soliton microcomb with an electronically detectable repetition rate.

4. CONCLUSION

In summary, we demonstrated a general architecture for efficient integration between two important integrated photonics platforms, i.e., a mature SOI waveguide platform and an emerging nonlinear III-V platform. We showcase efficient $\chi^{(3)}$-based optical frequency comb generation seamlessly integrated with Si PICs, while the same platform can be extended to incorporate other functions including $\chi^{(2)}$-based nonlinear photonics (e.g., second-harmonic generation). Importantly, the achieved low-loss AlGaAs-on-SOI enables efficient microcomb operation for Si PICs at power levels of only a few milliwatts, which is easily achievable with state-of-the-art standard III-V/Si heterogeneously integrated lasers. Our demonstration bridges mature SOI PICs and the superior nonlinear functionalities of III-V photonics, in addition to existing lasers, modulators, photodetectors, etc. The present result may provide a viable route towards fully functional nonlinear chips for miniaturized systems hosted in Si photonics and open new perspectives for related research and applications.
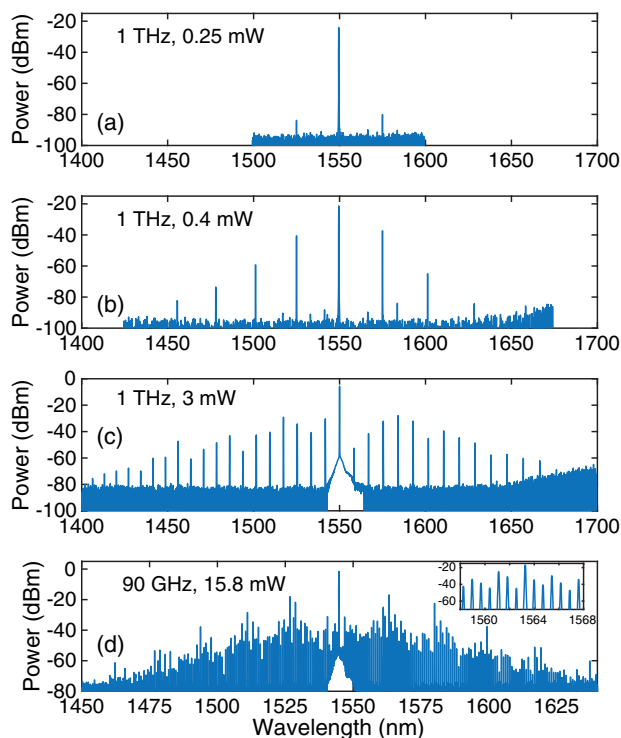

Fig. 4. Frequency comb spectra measured from Si waveguide edge coupler for two AlGaAs microrings: 1 THz ring at pump powers of (a) 0.25 mW, (b) 0.4 mW, and (c) 3 mW; (d) 90 GHz ring at pump power of 15.8 mW. Inset in (d): close-up of the comb spectrum in a selected wavelength range.

Disclosures. The authors declare no conflicts of interest.

Data Availability. All data generated or analyzed during this study are available upon reasonable request.

†These authors contributed equally to this paper.

REFERENCES

1. M. Lipson, "Guiding, modulating, and emitting light on silicon-challenges and opportunities," J. Lightwave Technol. **23**, 4222–4238 (2005).

2. R. Soref, "The past, present, and future of silicon photonics," IEEE J. Sel. Top. Quantum Electron. **12**, 1678–1687 (2006).

3. W. Bogaerts, R. Baets, P. Dumon, V. Wiaux, S. Beckx, D. Taillaert, B. Luyssaert, J. Van Campenhout, P. Bienstman, and D. Van Thourhout, "Nanophotonic waveguides in silicon-on-insulator fabricated with CMOS technology," J. Lightwave Technol. **23**, 401–412 (2005).

4. A. E.-J. Lim, J. Song, Q. Fang, C. Li, X. Tu, N. Duan, K. K. Chen, R. P.-C. Tern, and T.-Y. Liow, "Review of silicon photonics foundry efforts," IEEE J. Sel. Top. Quantum Electron. **20**, 405–416 (2013).

5. R. Jones, P. Doussiere, J. B. Driscoll, W. Lin, H. Yu, Y. Akulova, T. Komljenovic, and J. E. Bowers, "Heterogeneously integrated InP/silicon photonics: fabricating fully functional transceivers," IEEE Nanotechnol. Mag. **13**, 17–26 (2019).

6. Y. Arakawa, T. Nakamura, Y. Urino, and T. Fujita, "Silicon photonics for next generation system integration platform," IEEE Commun. Mag. **51**(3), 72–77 (2013).

7. D. Dai and J. E. Bowers, "Silicon-based on-chip multiplexing technologies and devices for peta-bit optical interconnects," Nanophotonics **3**, 283–311 (2014).

8. C. R. Doerr, "Silicon photonic integration in telecommunications," Front. Phys. **3**, 37 (2015).

9. W. Bogaerts, D. Pérez, J. Capmany, D. A. Miller, J. Poon, D. Englund, F. Morichetti, and A. Melloni, "Programmable photonic circuits," Nature **586**, 207–216 (2020).

10. N. Margalit, C. Xiang, S. M. Bowers, A. Bjorlin, R. Blum, and J. E. Bowers, "Perspective on the future of silicon photonics and electronics," Appl. Phys. Lett. **118**, 220501 (2021).

11. M. A. Foster, A. C. Turner, M. Lipson, and A. L. Gaeta, "Nonlinear optics in photonic nanowires," Opt. Express **16**, 1300–1320 (2008).

12. A. L. Gaeta, M. Lipson, and T. J. Kippenberg, "Photonic-chip-based frequency combs," Nat. Photonics **13**, 158–169 (2019).

13. T. J. Kippenberg, A. L. Gaeta, M. Lipson, and M. L. Gorodetsky, "Dissipative Kerr solitons in optical microresonators," Science **361**, eaan8083 (2018).

14. P. Marin-Palomo, J. N. Kemal, M. Karpov, A. Kordts, J. Pfeifle, M. H. P. Pfeiffer, P. Trocha, S. Wolf, V. Brasch, M. H. Anderson, R. Rosenberger, K. Vijayan, W. Freude, T. J. Kippenberg, and C. Koos, "Microresonator-based solitons for massively parallel coherent optical communications," Nature **546**, 274–279 (2017).

15. H. Hu, F. Da Ros, and M. Pu *et al.* et al., "Single-source chip-based frequency comb enabling extreme parallel data transmission," Nat. Photonics **12**, 469–473 (2018).

16. D. T. Spencer, T. Drake, and T. C. Briles *et al.* et al., "An optical-frequency synthesizer using integrated photonics," Nature **557**, 81–85 (2018).

17. D. T. Spencer, T. Drake, T. C. Briles, J. Stone, L. C. Sinclair, C. Fredrick, Q. Li, D. Westly, B. R. Ilic, A. Bluestone, N. Volet, T. Komljenovic, L. Chang, S. H. Lee, D. Y. Oh, M.-G. Suh, K. Y. Yang, M. H. P. Pfeiffer, T. J. Kippenberg, E. Norberg, L. Theogarajan, K. Vahala, N. R. Newbury, K. Srinivasan, J. E. Bowers, S. A. Diddams, and S. B. Papp, "Architecture for the photonic integration of an optical atomic clock," Optica **6**, 680–685 (2019).

18. M. A. Guidry, D. M. Lukin, K. Y. Yang, R. Trivedi, and J. Vučković, "Quantum optics of soliton microcombs," Nat. Photonics **16**, 52–58 (2022).

19. X. Ji, F. A. S. Barbosa, S. P. Roberts, A. Dutt, J. Cardenas, Y. Okawachi, A. Bryant, A. L. Gaeta, and M. Lipson, "Ultra-low-loss on-chip resonators with sub-milliwatt parametric oscillation threshold," Optica **4**, 619–624 (2017).

20. M. Zhang, C. Wang, R. Cheng, A. Shams-Ansari, and M. Lončar, "Monolithic ultra-high-Q lithium niobate microring resonator," Optica **4**, 1536–1537 (2017).

21. W. Xie, L. Chang, H. Shu, J. C. Norman, J. D. Peters, X. Wang, and J. E. Bowers, "Ultrahigh-Q AlGaAs-on-insulator microresonators for integrated nonlinear photonics," Opt. Express **28**, 32894–32906 (2020).

22. J. Liu, G. Huang, R. N. Wang, J. He, A. S. Raja, T. Liu, N. J. Engelsen, and T. J. Kippenberg, "High-yield, wafer-scale fabrication of ultralow-loss, dispersion-engineered silicon nitride photonic circuits," Nat. Commun. **12**, 2236 (2021).

23. M. W. Puckett, K. Liu, N. Chauhan, Q. Zhao, N. Jin, H. Cheng, J. Wu, R. O. Behunin, P. T. Rakich, K. D. Nelson, and D. J. Blumenthal, "422 million intrinsic quality factor planar integrated all-waveguide resonator with sub-MHz linewidth," Nat. Commun. **12**, 934 (2021).

24. J. Liu, A. S. Raja, M. Karpov, B. Ghadiani, M. H. P. Pfeiffer, B. Du, N. J. Engelsen, H. Guo, M. Zervas, and T. J. Kippenberg, "Ultralow-power chip-based soliton microcombs for photonic integration," Optica **5**, 1347–1353 (2018).

25. B. Stern, X. Ji, Y. Okawachi, A. L. Gaeta, and M. Lipson, "Battery-operated integrated frequency comb generator," Nature **562**, 401–405 (2018).

26. A. S. Raja, A. S. Voloshin, H. Guo, S. E. Agafonova, J. Liu, A. S. Gorodnitskiy, M. Karpov, N. G. Pavlov, E. Lucas, R. R. Galiev, A. E. Shitikov, J. D. Jost, M. L. Gorodetsky, and T. J. Kippenberg, "Electrically pumped photonic integrated soliton microcomb," Nat. Commun. **10**, 680 (2019).

27. B. Shen, L. Chang, J. Liu, H. Wang, Q.-F. Yang, C. Xiang, R. N. Wang, J. He, T. Liu, W. Xie, J. Guo, D. Kinghorn, L. Wu, Q.-X. Ji, T. J. Kippenberg, K. Vahala, and J. E. Bowers, "Integrated turnkey soliton microcombs," Nature **582**, 365–369 (2020).

28. W. Jin, Q.-F. Yang, L. Chang, B. Shen, H. Wang, M. A. Leal, L. Wu, M. Gao, A. Feshali, M. Paniccia, K. J. Vahala, and J. E. Bowers, "Hertz-linewidth semiconductor lasers using CMOS-ready ultra-high-Q microresonators," Nat. Photonics **15**, 346–353 (2021).

29. C. Xiang, J. Liu, J. Guo, L. Chang, R. N. Wang, W. Weng, J. Peters, W. Xie, Z. Zhang, J. Riemensberger, J. Selvidge, T. J. Kippenberg, and J. E. Bowers, "Laser soliton microcombs heterogeneously integrated on silicon," Science **373**, 99–103 (2021).

30. M. A. Foster, A. C. Turner, J. E. Sharping, B. S. Schmidt, M. Lipson, and A. L. Gaeta, "Broad-band optical parametric gain on a silicon photonic chip," Nature **441**, 960–963 (2006).

31. J. Leuthold, C. Koos, and W. Freude, "Nonlinear silicon photonics," Nat. Photonics **4**, 535–544 (2010).

32. C. Xiang, W. Jin, J. Guo, C. Williams, A. M. Netherton, L. Chang, P. A. Morton, and J. E. Bowers, "Effects of nonlinear loss in high-Q Si ring resonators for narrow-linewidth III-V/Si heterogeneously integrated tunable lasers," Opt. Express **28**, 19926–19936 (2020).

33. D. J. Moss, R. Morandotti, A. L. Gaeta, and M. Lipson, "New CMOS-compatible platforms based on silicon nitride and hydex for nonlinear optics," Nat. Photonics **7**, 597–607 (2013).

34. B. J. Eggleton, B. Luther-Davies, and K. Richardson, "Chalcogenide photonics," Nat. Photonics **5**, 141–148 (2011).

35. C. Xiong, W. Pernice, K. K. Ryu, C. Schuck, K. Y. Fong, T. Palacios, and H. X. Tang, "Integrated GaN photonic circuits on silicon (100) for second harmonic generation," Opt. Express **19**, 10462–10470 (2011).

36. C. Xiong, W. H. P. Pernice, X. Sun, C. Schuck, K. Y. Fong, and H. X. Tang, "Aluminum nitride as a new material for chip-scale optomechanics and nonlinear optics," New J. Phys. **14**, 095014 (2012).

37. U. D. Dave, B. Kuyken, F. Leo, S.-P. Gorza, S. Combrie, A. De Rossi, F. Raineri, and G. Roelkens, "Nonlinear properties of dispersion engineered InGaP photonic wire waveguides in the telecommunication wavelength range," Opt. Express **23**, 4650–4657 (2015).

38. C. Wang, C. Langrock, A. Marandi, M. Jankowski, M. Zhang, B. Desiatov, M. M. Fejer, and M. Lončar, "Ultrahigh-efficiency wavelength conversion in nanophotonic periodically poled lithium niobate waveguides," Optica **5**, 1438–1441 (2018).

39. D. M. Lukin, C. Dory, M. A. Guidry, K. Y. Yang, S. D. Mishra, R. Trivedi, M. Radulaski, S. Sun, D. Vercruysse, G. H. Ahn, and J. Vučković, "4H-silicon-carbide-on-insulator for integrated quantum and nonlinear photonics," Nat. Photonics **14**, 330–334 (2020).

40. D. J. Wilson, K. Schneider, S. Hönl, M. Anderson, Y. Baumgartner, L. Czornomaz, T. J. Kippenberg, and P. Seidler, "Integrated gallium phosphide nonlinear photonics," Nat. Photonics **14**, 57–62 (2020).

41. H. Jung, S.-P. Yu, D. R. Carlson, T. E. Drake, T. C. Briles, and S. B. Papp, "Tantala Kerr nonlinear integrated photonics," Optica **8**, 811–817 (2021).

42. M. Pu, L. Ottaviano, E. Semenova, and K. Yvind, "Efficient frequency comb generation in AlGaAs-on-insulator," Optica **3**, 823–826 (2016).

43. L. Chang, W. Xie, H. Shu, Q.-F. Yang, B. Shen, A. Boes, J. D. Peters, W. Jin, C. Xiang, S. Liu, G. Moille, S.-P. Yu, X. Wang, K. Srinivasan, S. B. Papp, K. Vahala, and J. E. Bowers, "Ultra-efficient frequency comb generation in AlGaAs-on-insulator microresonators," Nat. Communications **11**, 1331 (2020).

44. M. A. Afromowitz, "Refractive index of $Ga_{1-x}Al_xAs$," Solid State Commun. **15**, 59–63 (1974).

45. G. Stegeman, A. Villeneuve, J. Kang, J. Aitchison, C. Ironside, K. Al-Hemyari, C. Yang, C.-H. Lin, H.-H. Lin, G. Kennedy, R. S. Grant, and W. Sibbett, "AlGaAs below half bandgap: the silicon of nonlinear optical materials," Int. J. Nonlinear Opt. Phys. **3**, 347–371 (1994).

46. J. S. Aitchison, D. Hutchings, J. Kang, G. Stegeman, and A. Villeneuve, "The nonlinear optical properties of AlGaAs at the half band gap," IEEE J. Quantum Electron. **33**, 341–348 (1997).

47. S. Ho, C. Soccolich, M. Islam, W. Hobson, A. Levi, and R. Slusher, "Large nonlinear phase shifts in low-loss Al_xGa_{1-x} as waveguides near half-gap," Appl. Phys. Lett. **59**, 2558–2560 (1991).

48. K. Dolgaleva, W. C. Ng, L. Qian, and J. S. Aitchison, "Compact highly-nonlinear AlGaAs waveguides for efficient wavelength conversion," Opt. Express **19**, 12440–12455 (2011).

49. J. J. Wathen, P. Apiratikul, C. J. Richardson, G. A. Porkolab, G. M. Carter, and T. E. Murphy, "Efficient continuous-wave four-wave mixing in bandgap-engineered AlGaAs waveguides," Opt. Lett. **39**, 3161–3164 (2014).

50. J. McPhillimy, S. May, C. Klitis, B. Guilhabert, M. D. Dawson, M. Sorel, and M. J. Strain, "Transfer printing of AlGaAs-on-SOI microdisk resonators for selective mode coupling and low-power nonlinear processes," Opt. Lett. **45**, 881–884 (2020).

51. H. El Dirani, C. Monat, S. Brision, N. Olivier, C. Jany, X. Letartre, M. Pu, P. D. Girouard, L. H. Frandsen, E. Semenova, L. K. Oxenløwe, K. Yvind, and C. Sciancalepore, "SiNOI and AlGaAs-on-SOI nonlinear circuits for continuum generation in Si photonics," Proc. SPIE **10535**, 1053508 (2018).

52. J. Chiles, N. Nader, E. J. Stanton, D. Herman, G. Moody, J. Zhu, J. C. Skehan, B. Guha, A. Kowligy, J. T. Gopinath, K. Srinivasan, S. A. Diddams, I. Coddington, N. R. Newbury, J. M. Shainline, S. W. Nam, and R. P. Mirin, "Multifunctional integrated photonics in the mid-infrared with suspended AlGaAs on silicon," Optica **6**, 1246–1254 (2019).

53. E. J. Stanton, L. Chang, W. Xie, A. Malik, J. Peters, J. Chiles, N. Nader, G. Navickaite, D. Sacchetto, M. Zervas, K. Srinivasan, J. E. Bowers, S. B. Papp, S. W. Nam, and R. P. Mirin, "On-chip polarization rotator for type I second harmonic generation," APL Photon. **4**, 126105 (2019).

54. E. J. Stanton, J. Chiles, N. Nader, G. Moody, N. Volet, L. Chang, J. E. Bowers, S. W. Nam, and R. P. Mirin, "Efficient second harmonic generation in nanophotonic GaAs-on-insulator waveguides," Opt. Express **28**, 9521–9532 (2020).

55. B. Kuyken, M. Billet, F. Leo, K. Yvind, and M. Pu, "Octave-spanning coherent supercontinuum generation in an AlGaAs-on-insulator waveguide," Opt. Lett. **45**, 603–606 (2020).

56. G. Moille, L. Chang, W. Xie, A. Rao, X. Lu, M. Davanco, J. E. Bowers, and K. Srinivasan, "Dissipative Kerr solitons in a III-V microresonator," Laser Photon. Rev. **14**, 2000022 (2020).

57. H. Shu, B. Shen, L. Chang, W. Xie, J. Qin, M. Jin, X. Zhang, X. Wang, and J. E. Bowers, "Mode-locked dark-pulse Kerr combs in normal-dispersion AlGaAs-on-insulator microresonators," in *Conference on Lasers and Electro-Optics*, (Optical Society of America, 2021), paper STu2G.4.

58. T. J. Steiner, J. E. Castro, L. Chang, Q. Dang, W. Xie, J. Norman, J. E. Bowers, and G. Moody, "Ultrabright entangled-photon-pair generation from an AlGaAs-on-insulator microring resonator," PRX Quantum **2**, 010337 (2021).

59. S. Zhang, J. M. Silver, L. Del Bino, F. Copie, M. T. Woodley, G. N. Ghalanos, A. Ø. Svela, N. Moroney, and P. Del'Haye, "Sub-milliwatt-level microresonator solitons with extended access range using an auxiliary laser," Optica **6**, 206–212 (2019).

60. A. B. Matsko, A. A. Savchenkov, D. Strekalov, V. S. Ilchenko, and L. Maleki, "Optical hyperparametric oscillations in a whispering-gallery-mode resonator: threshold and phase diffusion," Phys. Rev. A **71**, 033804 (2005).